Size effect in particle debonding: Comparisons between Finite Fracture Mechanics and Cohesive Zone Model

Timothée Gentieu[a,c,*], Julien Jumel[a], Anita Catapano[b], James Broughton[c]

[a] *Université de Bordeaux, I2M CNRS UMR 5295, F-33400 Talence, France*
[b] *Bordeaux INP, Université de Bordeaux, I2M CNRS UMR 5295, F-33400 Talence, France*
[c] *Oxford Brookes University (OBU), Wheatley Campus, OX331HX, UK*

Abstract

The present study aims at describing the debonding phenomenon of a particle embedded in an elastic matrix. Two types of fracture mechanics approaches are developed and compared in this context. The phenomenon is analytically described using a Finite Fracture Mechanics (FFM) approach, while numerical simulations are performed using a Cohesive Zone Model (CZM) to describe the decohesion process. Both methods rely on two mechanical parameters: the interface strength, σ_{max} and the fracture energy, G_c, of the interface. Both modelling approaches produce results that show larger particles tend to debond before smaller ones which is captured by both models, although noticeable differences are observed, especially concerning the relationship between the critical load and the particle radius: in the framework of the FFM, the critical load is inversely proportional to the square root of the particle radius while when using CZM, the critical load is inversely proportional to the particle radius.

1. Introduction

Particle reinforced composite materials are used in a large variety of industrial applications such as automotive, aeronautics, or aerospace to satisfy various requirements. Many different types of materials are combined to obtain composite materials exhibiting better mechanical performances than the ones of its constituents. The addition of rigid particles, e.g. metallic or ceramic, in a more compliant matrix is a common practice to stiffen the polymer matrix. The mechanical properties of the resulting composite material depend on the mechanical properties of the components (elastic moduli, strength), their geometries (shape of the inclusions), and their interactions (adhesion between the matrix and the inclusion, contrast between the mechanical properties). Adding particles could also be beneficial for enhancing material toughness. However, multiple dissipative damage mechanisms have been invoked to explain this. For example, Gent observed cavitation in the vicinity of the particle [1]. An exaustive review of particle reinforced polymers is presented by Fu et al [2]. In [2], several toughening mechanisms are introduced: crack front bowing (or crack pinning), crack-tip blunting, diffused matrix shear yielding, micro-cracking, crack deflection by hard particles, micro-shear banding, breakage of particles. The effect of rigid particle debonding in thin films was studied also in [3].

Three main types of microcracks are often observed in composite polymers filled with rigid particles: particles fracture, microcracks/plasticity developing in the matrix and mi-

*Corresponding author. Tel.: +33540006220
Email address: timothee.gentieu@u-bordeaux.fr (Timothée Gentieu)

crovoids nucleation caused by interfacial debonding between the particles and the matrix [4]. According to [4], the damage corresponding to the first two is generally much less than the one associated to the third type. Interfacial debonding between particles and matrix is the first damage mechanism to be triggered and is considered as the main toughening mechanism [5]. Among several parameters relating to particle debonding, particular attention is drawn to the geometric aspect of particle size. Indeed, a clear particle size effect described by Fu et al [2], who cites observations in [6] that relate to both an increase in toughness of an epoxy resin reinforced with increasing spherical particle size, and a decrease in strength. As reviewed in [2], this might not be true for nanosize particles. Most of the studies carried out on the particle size effect observe this phenomenon indirectly, e.g. through the variation of homogenised properties.

The elastic field around a spherical particle embedded in an infinite matrix can be determined analytically assuming that the adhesion between the particle and the matrix is perfect (viz. rigid contact). When the particle is more rigid than the matrix, the peak interface stresses are located at the pole of the particle, parallel to the loading direction. An analytical expression of the maximal stress (σ_d) has been derived by Goodier [7] with respect to the remote stress applied to the material (σ_∞):

$$\begin{aligned}\frac{\sigma_d}{\sigma_\infty} = 1 - & \frac{G_m - G_p}{(7-5\nu_m)\,G_m + (8-10\nu_m)\,G_p} \\ & \cdot \frac{(1-2\nu_p)\,(7-5\nu_m)\,G_m + (1+5\nu_p-5\nu_m\nu_p)\,2G_p}{(1-2\nu_p)\,2G_m + (1+\nu_p)G_p} \\ & + \frac{\left[(1-\nu_m)\,\frac{1-\nu_p}{1+\nu_m} - \nu_p\right] G_p - (1-2\nu_p)\,G_m}{(1-2\nu_p)\,2G_m + (1+\nu_p)\,G_p}.\end{aligned} \tag{1}$$

with G_m and ν_m being the matrix shear modulus and Poisson's ratio, and G_p and ν_p the particle shear modulus and Poisson's ratio respectively. According to Eq. 1, it should be notice that peak stress value does not depend on the size of the particle. It is observed experimentally that the damage initiation stress depends on particle size [8] whereas the stress concentration does not. Lauke in [9] asks two crucial questions about the debonding parameters for a spherical particle: "First: Is the debonding stress, σ_c, dependent on the particle diameter? And second: Is the interface debonding energy, G_c, a material parameter, or is it dependent on geometrical conditions, such as different curvatures for different particle sizes, near the interface?".

Gent tried to analytically describe the debonding of a spherical particle [10]. He used Griffith's criterion on a sphere with a debonded patch at its pole (modelled as a zone of non-carrying load). He obtained the following debonding stress expression:

$$\sigma_c^2 = \frac{8\pi G_c E_m}{3kR\sin(2\theta)}, \tag{2}$$

E_m being matrix Young's modulus, k a numerical parameter, R the radius of the particle, and θ the angle of the debonded patch. The value of the applied stress becomes very high for debonding angles of θ around 0° and 90°. A minimum is reached for a debonding angle of 45° (Gent gives a value for the dimensionless numerical parameter $k = 2$ based on a comparison with another case study):

$$\sigma_c^2 = \frac{4\pi G_c E_m}{3R}. \tag{3}$$

For a hydrostatic loading, it has been demonstrated by several authors [5], [9], [11], [12] [13] using the Linear Elastic Fracture Mechanics (LFEM) approach, that for a particle embedded in a much softer infinite matrix (viz. rigid spherical particle assumption), the critical stress at the interface needed to debond the particle from the matrix is given by the relationship:

$$\sigma_{dec} = \sqrt{\frac{G_c}{R}\frac{4E_m}{1+\nu_m}}. \tag{4}$$

This expression indicated that the stress provoking particle decohesion, σ_{dec}, is proportional to the inverse of the square root of the radius of the particle R. Since only an energy-based criterion has been applied to describe crack propagation in this situation, the interface strength, σ_c, does not influence the decohesion process. The authors tried to describe the debonding of nanoparticles, but as stated by Salviato et al in [13], since no size limitations have been formulated in the model, the equations are valid both for nanosized and microsized particles. Chen et al in [5] tried to describe the energy dissipation by rigid particle debonding in a viscoelastic matrix. Williams in [11] tried to determine the toughness of a composite as function of the volume fraction of nano and micro particles with two different damage mechanisms, debonding and plastic voids growth. Salviato, Zappalorto and Quaresimin in [13], [14], [12], [15] determined the debonding stresses for nanoparticles coated with interphases under different loading conditions. Lauke in [9] tried to determine the toughness of a particle reinforced polymer and he cited Eq. 4 from all the previously cited works. Finally, it is noteworthy that considering the limit case of a rigid particle, in an infinite matrix, with no interphase nor surface stress, the crack onset criterion obtained always coincides to Eq. 4.

The present article aims to analyse the debonding process of a single particle embedded in an elastic matrix by using two different approaches: the Finite Fracture Mechanics approach (FFM) and Cohesive zone Model (CZM). The objective is to set an analytical relationship between the particles size and the debonding evolution. In Sections 2 and 3, the Finite Fracture Mechanics (FFM) and Cohesive Zone Models (CZM) will respectively be described in the context of spherical particle debonding. Then, Section 4 is dedicated to the debonding of a spherical particle under hydrostatic loading. Section 5 focuses on the debonding of a spherical particle under uniaxial tensile loading. The FFM and CZM will be compared and interpreted in Section 6. Finally, the case of a angular particle will be studied and compared to previous results in Section 7.

The case study for the spherical particle debonding is one single particle embedded in a cylinder of matrix. The geometry of the Representative Volume Element (RVE) is the one presented in Fig. 1. The radius of the sphere is equal to one tenth of the diameter of the cylinder: $R = L/10$, which corresponds to a volume fraction $\phi = 0.0053$. The geometry is reduced to a 2D structure by axisymmetry, and then only half of the geometry is modelled by using a mirror symmetry along the horizontal axis. The following assumptions always apply to the present study:

1. the material behaviour of both particles and matrix is linear elastic;
2. the interface is infinitely stiff.

In any case the moduli associated with the particle are those of the boron-carbide while the ones of the matrix correspond to a "standard" epoxy resin (see Table 1).

2. Finite Fracture Mechanics (FFM) applied to particle debonding: coupled stress and energy criteria

For analysing crack onset and propagation with the FFM approach, the system elastic response is first evaluated considering several decohesion lengths along the particle contour. First considering a non-damaged situation (no decohesion), the FFM aims at determining the critical load responsible for crack onset over a finite length (or surface for the 3D case) ΔA. According to Leguillon [16], none of the traditional stress or energy criteria alone (i.e. LEFM, Griffith's theory) are sufficient to describe crack onset and propagation. Leguillon states that both criteria have to be simultaneously fulfilled for a crack to develop:

$$\begin{cases} \sigma_{eq} \geq \sigma_{max}, \\ \bar{G}\left(\Delta A\right) \geq G_c; \end{cases} \tag{5}$$

with σ_{eq} a scalar equivalent stress and $\bar{G}$ the incremental energy release rate (IERR). More details related to the definition of these quantities are given below.

2.1. Stress criterion

Considering only an ultimate stress criterion, two surfaces are considered debonded when the interfacial stress reaches a critical value σ_{max}, which is a material parameter of the interface:

$$\sigma_{eq} \geq \sigma_{max}. \tag{6}$$

The cohesive stresses at the interface being a vector, one needs to define a scalar equivalent stress σ_{eq} to be compared to the interfacial strength. Several approaches exist in the literature, like the one of the maximal principal stress [17] or the quadratic average [18]. In the framework of this study, we will use a simple quadratic expression based on [18]:

$$\sigma_{eq} = f(\sigma_{ij}) = \sqrt{\langle \mathrm{sgn}\left(\sigma\right) |\sigma|^2 + |\tau|^2 \rangle_+}, \tag{7}$$

which is a quadratic average of the normal and tangential stresses at the interface. The sign of the normal interfacial stress σ is introduced here so that a compressive stress state does not induce a favourable contribution to debonding. The use of the positive part implies that σ_{eq} is null when the compressive stress state is predominant, which is a rather severe condition. The stress criterion can then be applied using two different methods:

- the point method (PM) introduced by Leguillon [16], where the stress is evaluated at each position along the expected crack path, and then compared to the strength:

$$\sigma_{eq}(x) > \sigma_{max}, \ \forall \ x \in \Omega_c; \tag{8}$$

- the line method (LM) introduced by Cornetti et al [19], where the stress is averaged along the crack propagation path, and then compared to the strength:

$$\frac{1}{\Delta A} \int_{\Omega_c} \sigma_{eq}(\tilde{x}) \mathrm{d}\tilde{x} > \sigma_{max} \tag{9}$$

The PM will be employed for this study.

2.2. Energy criterion

An energy balance equation must be verified for a crack to propagate along the interface, considering the state of the system before and after crack propagation :

$$\Delta W_p + \Delta W_k + G_c\ \Delta A = 0, \tag{10}$$

where ΔW_p and ΔW_k are the variation of the potential energy and kinetic energy of the system respectively, G_c is the critical fracture energy per unit surface, and ΔA is the fractured surface created during the decohesion process. When a crack propagates in the system the kinetic energy increases so that $\Delta W_k \geq 0$. Then to satisfy the energy equilibrium, Eq. 10 becomes:

$$-\frac{\Delta W_p}{\Delta A} \geq G_c. \tag{11}$$

Now, according to Weißgraeber et al [17], one can introduce the concept of IERR $\bar{G}$. The crack propagates when $\bar{G}$ reaches the fracture energy (per unit surface) G_c, also called surface toughness:

$$\bar{G} = -\frac{\Delta W_p}{\Delta A} \geq G_c. \tag{12}$$

This IERR clearly differs from the standard Griffith's criterion where the energy release rate $G = -\delta W_p/\delta A$ is compared to the fracture energy for each crack tip position. As defined by [17], the IERR is in fact the "average" of the energy release rate along the crack path so that the energy balance equation is evaluated over the whole crack propagation process:

$$\bar{G}(\Delta A) = \frac{1}{\Delta A}\int_{\Delta A} G(\tilde{A})\mathrm{d}\tilde{A}. \tag{13}$$

The energy release rate might be evaluated using the Virtual Closure Crack Technique (VCCT) [20]. This method is cited by Weißgraeber et al [17] as a way to determine the energy release rate for FFM. Cho et al [21] used this method in the case of a single spherical particle embedded in a polymer matrix to explain the size effect. Garcia et al [18] used it for a spherical particle in the FFM context. In the present study, another strategy is employed. The energy release rate is the change in potential energy of the system as the crack propagates. As schematically illustrated in Fig. 2 (a), the loss of potential energy of a system loaded in uniaxial tension is equal to the shaded area between the load-displacement curves before (in blue) and after (in orange) crack propagation. From this consideration, it is possible to evaluate the energy release rate as a function of the evolution of the compliance of the structure. Indeed, deriving the expression of the potential energy in Eq. 12, and denoting P the load applied to the structure, U the associated displacement, and $C = U/P$ the compliance of the body, we are now able to calculate the energy release rate based on the compliance evolution of the body:

$$G = \frac{1}{2}P^2\frac{\mathrm{d}C}{\mathrm{d}A} = P^2 G_{norm}, \tag{14}$$

where G_{norm} being the energy release rate normalised with the applied load. In the case of a spherical particle with a radius R embedded in a matrix, and θ the debonding angle,

the normalised energy release rate becomes:

$$G_{norm} = \frac{1}{2} \frac{\mathrm{d}C}{2\pi R^2 \sin(\theta)\, \mathrm{d}\theta}. \tag{15}$$

To numerically determine G_{norm}, an elastic FE calculation is employed as the crack tip position is manually moved so that the evolution of the compliance provides the energy release rate.

The same method is employed for the hydrostatic loading case. The potential energy in this case the shaded area between the pressure-volume change curves before and after crack propagation (Fig. 2 (b)). To keep the same formalism as previously defined for uniaxial tension, a compliance c is defined as the ratio of the dilatation ΔV over the pressure p, and the energy release rate becomes:

$$G = \frac{1}{2} p^2 \frac{\mathrm{d}c}{\mathrm{d}A} = p^2 G_{norm}, \tag{16}$$

This procedure will be more precisely developed in Sections 4 and 5 for the hydrostatic and uniaxial tensile loading cases.

2.3. Coupled criterion

The coupled criterion states that for a crack of a finite size ΔA, both the stress and energy criteria have to be simultaneously fulfilled along the crack path to allow the crack opening. Such a criterion leads to the following minimisation problem:

$$P_c = \min_{P,\ \Delta A} \left\{ P \mid \sigma_{eq}(x) \geq \sigma_{max},\ x \in \Omega_c \text{ and } \bar{G}(\Delta A) \geq G_c \right\} \tag{17}$$

The solution to problem 17 indicates the minimum load that fulfills both criteria and the size of the crack ΔA. In the present work, the crack can only propagate along the interface between the spherical particle and the matrix. Therefore, for the sake of simplicity, the axisymmetry can be used to reduce the 3D problem to a 2D one. The problem 17 then becomes:

$$P_c = \min_{P,\ \theta} \left\{ P \mid \sigma_{eq}(\tilde{\theta}) \geq \sigma_{max},\ \tilde{\theta} \in \Omega_c \text{ and } \bar{G}(\theta) \geq G_c \right\}. \tag{18}$$

3. The Cohesive Zone Model applied to particle debonding

For numerical evaluation of interface decohesion in a Finite Elements (FE) context, CZM are commonly used. A CZM is an interface separation law linking the cohesive stress components at the interface and the displacement jump between the two surfaces created. Multiple traction-separation law shapes have been developed such as bilinear, trilinear, exponential, etc. Triangular/bilinear CZM law is generally used to describe brittle failure process.

The bilinear CZM is represented in Fig 3. It basically relies on two mechanical parameters: interface strength σ_{max} and interface fracture energy G_c (i.e. the shaded area under the traction-separation curve). The introduction of these two parameters implies a critical displacement u_c which, according to Leguillon [16], is not a material parameter but a structural one. The critical displacement value, u_c, can be determined as a function of σ_{max} and G_c as follows:

$$u_c = \frac{2G_c}{\sigma_{max}} \tag{19}$$

The fracture energy of the traction-separation law is chosen to be 100 $J.m^{-2}$ and its strength 50 MPa to be consistent with the values used for the FFM analysis. For the bilinear law used in the software Ansys, based on Alfano & Crisfield work [22], the first part of the curve shows a linear elastic behaviour. A careful attention must be given to its slope as it softens the global elastic properties of the composite. The stiffness of the interface is selected to be high enough so that the global stiffness of structure is not modified whatever the particle size is. Then, once the interfacial strength is reached, a linear softening occurs until the stress completely vanishes and the interface is considered to be completely debonded.

The mesh and boundary conditions are depicted in Fig. 4. The mesh is refined at the particle/matrix interface to suppress all mesh size effects. 180 interface elements are introduced so that each element represents 0.5° of angle. The following boundary conditions are applied to ensure mirror symmetries of the RVE:

$$\begin{cases} U_x(x=0)=0, \\ U_y(y=0)=0. \end{cases} \tag{20}$$

Uniform constant displacement conditions are imposed at the boundary of the mesh to reproduce either hydrostatic or uniaxial loading conditions. The reference stress applied to the RVE is obtained by summing all the nodal reaction forces where the displacement loading has been applied divided by the transverse surface area of the RVE.

4. Debonding of a spherical particle under hydrostatic tensile loading

The first reference case to be analysed is the debonding of a spherical particle from the matrix under hydrostatic tensile loading. Both the FFM approach and the CZM are employed. Concerning the boundary conditions (BCs), a displacement U is applied on every external surface on the structure (the imposed displacement is represented in Fig. 4 with the green and orange arrows):

$$\begin{cases} U_x(x=L)=U, \\ U_y(y=L)=U. \end{cases} \tag{21}$$

This particular loading case can lead to two different configurations: either the load is not sufficient to debond the particle from the matrix and the whole interface is still bonded (Fig. 5 (a)) or the load is sufficiently high to instantaneously trigger complete debonding of the particle (Fig. 5 (b)).

As stated in Section 2, in the framework of FFM, the evaluation of the remote stress responsible for debonding correspond to the minimum stress that fulfils both the stress and energy criteria, i.e. Eqs. 8 and 12 respectively.

An elastic FE calculation of the RVE considering perfect bonding (viz. rigid interface) between matrix and particle determines the relationship between the remote stress and the stress at the interface. The evaluation of the critical remote stress that fulfils the stress criterion is then straightforward (Eq. 8).

Concerning the energy criterion, the hydrostatic compliance c for both bonded and debonded situations is calculated with FE computation, and the normalised energy release rate is derived from the evolution of the compliance (Eq. 16). Then, the critical remote stress that fulfils the energy criterion (Eq. 12) is determined with the relation:

$$\sigma_{\infty c} = \sqrt{\frac{\Delta A\, G_c}{\Delta A\, G_{norm}}} = \sqrt{\frac{G_c}{G_{norm}}} \tag{22}$$

The same situation can then be described by introducing a cohesive zone along the particle/matrix interface.

This procedure is repeated for multiple particle radii (ranging from 10 μm to 2000 μm). The R/L ratio being kept constant for all calculations. The results are plotted in Fig. 6 (a). The magenta dots represent the FFM predictions, the blue ones the CZM. The green solid line corresponds to that of the energy-based criterion Eq. 4. As a result, we observe that for small particles, the stress responsible for particle debonding increases when the particle size decreases. For larger particles, this stress reaches a plateau value. These observations hold for both FFM and CZM. The analytical expression derived in Eq. 4 matches very well with the results obtained from the FFM for small particles. We can deduce that for particles whose radius is less than 400 μm, according to both FFM and CZM approaches, the energy criterion controls the debonding onset. On the contrary, when particle radius is larger than this threshold value, the stress criterion is the predominant one.

The critical remote stress vs the particle radius can be represented on a log-log scale to help visualise the transition from $1/\sqrt{R}$ to stationnary evolutions (Fig. 6 (b)) as predicted with the FFM approach. On the other hand, there is also a clear difference between the FFM and CZM approaches, since the remote stress for small particle sizes is proportional to $1/R$ in the (former) case. For larger particles, both models reach the same plateau value. The two regimes intersect at exactly the same particle radius for both models.

5. Debonding of a spherical particle under uniaxial tensile loading

In this case, a vertical displacement U is imposed at the upper boundary of the RVE only in order to obtain a far field uniaxial stress state (the imposed displacement is represented in Fig. 4 with the orange arrows only). The right boundary ($x = L$) is left unconstrained so that the loading conditions can be summed up with:

$$U_y(y = L) = U \tag{23}$$

For FFM analysis, the evolution of the system compliance is evaluated for several debonding angles with an increment θ_{inc} equal to 1° from fully bonded to fully debonded situation. The compliance is evaluated using the same methodology again: the imposed displacement, U, being known, the the reaction forces, P, on the top boundary is obtained by summing the nodal reaction forces (see Fig. 7 (a)). Then, the derivative of the compliance is calculated using finite difference scheme between the successive calculation steps: $\mathrm{d}C/\mathrm{d}A = \Delta C/\Delta A$ (see Fig. 7 (b)). Recalling Eq. 15, G_{norm} is calculated from the evolution of the compliance for every debonding angle, and for different particle sizes (see Fig. 8 (a)). The normalised energy release rate is found to be maximum for 45° for every particle size and the specific value of G_{norm} appears to be dependent on the particle radius. However, it is possible to find a quantity that is scale-independent if the normalised energy release rate is multiplied by R^3, in which case all the curves are superimposed (see Fig. 8 (b)). The normalisation procedure allows the compliance evolution to be evaluated for only one particle size to determine the normalised energy release rate for all particle sizes (in accordance with [23]).

Using this energy criterion, it is possible to determine the remote stress which provokes

the debond onset and the rapide decohesion of the particle over an angle θ, $\sigma_{\infty c}(\theta)$:

$$\bar{G}(\Delta A) = G_c, \tag{24}$$

$$\frac{1}{\Delta A}\int_{\Delta A} G(\tilde{A})\mathrm{d}\tilde{A} = G_c, \tag{25}$$

$$\frac{1}{\Delta A}\int_{\Delta A} P_c^2(\Delta A) G_{norm}(\tilde{A})\mathrm{d}\tilde{A} = G_c, \tag{26}$$

$$\frac{1}{\Delta A} P_c^2(\theta)\int_{\tilde{\theta}=0}^{\theta} G_{norm}(\tilde{\theta}) 2\pi R^2 \sin(\tilde{\theta})\mathrm{d}\tilde{\theta} = G_c, \tag{27}$$

$$P_c^2(\theta) = \frac{\Delta A\ G_c}{\displaystyle\int_{\tilde{\theta}=0}^{\theta} G_{norm}(\tilde{\theta}) 2\pi R^2 \sin(\tilde{\theta})\mathrm{d}\tilde{\theta}}, \tag{28}$$

$$\sigma_{\infty c}(\theta) = \frac{1}{S}\sqrt{\frac{\Delta A\ G_c}{2\pi R^2 \displaystyle\int_{\tilde{\theta}=0}^{\theta} G_{norm}(\tilde{\theta})\sin(\tilde{\theta})\mathrm{d}\tilde{\theta}}}, \tag{29}$$

where $\Delta A = 2\pi R^2\,(1-\cos(\theta))$ is the crack surface, and $S = \pi(L/2)^2$ is the cross section of the representative element, under revolution symmetry assumption. The integral of G_{norm} only depends on one variable $\tilde{\theta}$ and is numerically evaluated using a trapezoidal rule.

Then, for FFM analysis, the stress criterion should be evaluated. The stress field along the particle/matrix interface, considered as rigid, is determined using linear elastic FE calculation. The stresses at the particle/matrix interface are obtained for every angular position along the interface and are plotted in Fig. 9. For spherical particles, the stress concentration only depends on the elastic contrast between the particle and the matrix and far field stress state. It is independent of the size of the particle. The evolution of the remote stress responsible for debonding according to the stress criterion is also reported in Fig. 10. According to the FFM approach, both energy and stress criterion should be triggered for a crack to initiate. Then, the critical stress responsible for the debonding onset is the minimum stress that fulfils both criteria. This minimum value is also associated with a specific angle value, which actually corresponds to the debonding angle θ after onset. It is easy to observe from Fig. 10 that, with respect to the angular position, the stress criterion leads to a continuously increasing function, whilst, for all particle sizes, a local minimum is observed at ca 58° for all curves obtained with the energy criterion. Therefore, two different regimes can be observed. The first one is obtained when the curves of the stress and energy criteria intersect before the energy criterion minimum. For this regime, the minimum stress that fulfills both criteria is reached at the intersection of both curves. After this point (for smaller particles), the onset of decohesion is driven by the energy criterion rather than the stress one.

It is then possible to plot the remote stress responsible for debonding onset against the particle radius (Fig. 11 (a)). For small particles (R smaller than around $100\mu m$), the energy criterion is dominant and the critical remote stress increases with decreasing particle size. For particles whose radii are larger than $600\mu m$, the evolution of the critical remote stress reaches an asymptotic stationary evolution, as the stress criterion governs the outcome. For intermediate particles size ($100\mu m < R < 600\mu m$) smooth transition between the two regimes is observed where both interface strength and fracture energy influence the debonding conditions.

Similar analysis is then carried out numerically using CZM to describe the particle/matrix interface separation behaviour. Very similar trends to the one obtained with

the FFM approach are observed (see Fig. 11 (a)). For now, we focus on the dependence of the critical remote stress and decohesion angle as a function of the particle radius, R. This evolution has also been plotted in a log-log scale for comparison with the results obtained with the FFM method (Fig. 11 (b)). Again, two asymptotic regimes are observed. For the largest considered particle sizes, the critical remote stress obtained with both methods reaches the same plateau value corresponding to the situation when decohesion is driven by the interface strength. For the smallest particles, however, as previously observed under a hydrostatic loading condition, two different asymptotic regimes are observed. With the FFM, the critical stress is proportional to $1/\sqrt{R}$ while with the CZM, it is proportional to $1/R$.

6. Discussion on the physical interpretations for both models

Overall, both models (FFM and CZM based) provide the same outcomes: large particles tend to debond prior to smaller ones, which corroborates existing experimental findings. However, quantitatively, the results obtained by both numerical simulations and FFM method do not match. First, it is to be noted that for the hydrostatic loading,the results exactly match the trend lines, whereas for the uniaxial loading only asymptotic behaviours are observed. Two different asymptotic behaviours are described, one for small particles and one for large particles.

For large particles, a plateau value is reached for the critical remote stress responsible for debonding onset $\sigma_{\infty c}$. This value is the exact one for which the stress at the particle/matrix boundary exceeds the interfacial strength. It is the same one for both the FFM and the CZM. It means, that for large particles, debonding is governed by the stress criterion.

For small particles, the critical stress $\sigma_{\infty c}$ is proportional to $1/\sqrt{R}$ in the framework of FFM and to $1/R$ when using the CZM approach. In the case of hydrostatic loading, asymptote matches that of the analytical approximation, based only upon the energy-based criterion from Eq. 4. This means that the debonding of small particles is governed by the energy criterion with the FFM. The evolution in $1/\sqrt{R}$ of $\sigma_{\infty c}$ is the one predicted by the energy criterion. However, with the CZM, the critical stress is proportional to $1/R$ which implies that the fracture process might not be properly captured by the simple linear fracture mechanics analysis. Indeed, from the numerical simulation with the CZM, not only the crack onset and propagation can be captured but also the development of the interface damage ahead of the crack tip. It should be remembered that with the FFM method, only infinitely small damage process zones are considered at the crack tip. For large particles, the size of the process zone is small compared to the particle dimension whatever the position of the crack tip is. In this case, the effect of interface behaviour nonlinearity is negligible in both stress and energy based analysis.

To the contrary, for small particles, a large process zone is observed ahead of the crack tip with the CZM. This means that the assumptions of the LEFM are not verified anymore and that the energy is dissipated not only at the crack tip but around the whole particle before full decohesion is reached at the pole of the particle. With the CZM, much higher critical stress is observed compared to the one predicted with the FFM approach, the difference being more pronounced as long as the particle reduces. This effect is simply attributed to the increase of the damage process zone observed with the CZM at the crack onset. For the smallest particle considered here, the process zone at damage onset is extended to almost the whole interface. These results question the capacity of both FFM method and CZM to properly capture the particle decohesion process since capturing the exact extent of process zone and/or shape of interface separation law seems difficult

experimentally, despite the fact that they clearly control the critical stress scaling law for small particles.

7. Debonding of an angular particle under uniaxial tensile loading

In the previous sections, the debonding of perfectly spherical particles has been described with the FFM and the CZM. However, some applications of particle reinforced material require the use of angular particles rather than spherical ones. In order to analyse the debonding phenomenon of a more generic particle shape, the example of a boron carbide particle embedded in an epoxy matrix has been analysed. First, the angular particle has been observed with Scanning Electron Microscopy (SEM), see Fig. 12. This particle shows facets and sharp angles than can have a significant influence on the behaviour of the composite material, as this type of geometry can introduce significant stress concentrations. A typical 2D geometry of an angular particle has been extracted from Fig. 12. For the sake of brevity, this last example is analysed by using only the CZM approach. In this framework, to avoid stress singularities, all the sharp angles of the particle were rounded with small fillets. Indeed, CZM requires rounded angles because the stress singularities induce a mesh size effect (the finer the mesh, the higher the stress concentration) that can falsify the debonding stress.

The revolution symmetry condition cannot be applied to angular particles hence, to keep a 2D analysis framework, plane strain assumption is introduced. This situation is usually considered for cross sectional analysis of composite materials, but it will also give valuable physical insight into the debonding process of angular inclusions. More quantitative analysis would necessitate full 3D calculations. Taking advantage of the 2D situation, we will now concentrate on the influence of both particle size and particle orientation on the critical stress leading to particle decohesion (see Fig. 13). To compare these results with a reference situation, the same calculation were performed considering circular (cylindrical) inclusion. The radius of the inclusion is denoted R again, for the RVE but the new volume fraction, $\phi = 0.0314$, is used for both the angular and circular inclusion (see Fig. 14). The equivalent radius of the angular inclusion R_{eq} is defined as the radius of the circular inclusion leading to the same volume fraction.

The CZM simulations are performed for various particle size and orientation to determine the critical remote stress responsible for the debond onset. The mesh and boundary conditions of the FE analysis are described in Fig. 15. A uniaxial tensile loading is applied to the RVE, and the boundary conditions can be mathematically formalised as follows:

$$\begin{cases} U_x(x=0, y=0) = 0, \\ U_y(y=0) = 0, \\ U_y(y=L) = U. \end{cases} \tag{30}$$

Also in this case, the scale effect was analysed by performing homothety operations on the RVE. First, the particle with a 0° orientation is studied. The critical remote stress responsible for the debonding onset is determined and plotted against the size of the particle (expressed through the equivalent radius R_{eq}) in Fig. 16. The results are compared to the one obtained with the circular inclusion. It can be observed that the size effect remains very significant and small particles tends to debond at higher remote stresses than larger ones whether they are cylindrical or they exhibit polyhedral nature. As observed for the spherical particle, the critical remote stress reaches a stable value for large particles when we consider a circular inclusion. However, for the angular inclusion, the critical remote stress for large particles slightly decreases with the increase in particle size. Figs. 17 and 18

report the critical remote onset stresses for the angular particle as a function of particle size and angular position. A similar large/small particle transition regime is observed whatever the orientation of the particle. However, while stationary critical remote stress is observed at orientation 0° for large particle, a significant decrease is observed for other angular position, the most severe configuration being 90°. For this configuration, almost constant decrease of the remote critical stress is observed. This clearly indicates that the crack onset is not only controlled here by the dimension of the particle but the small curvature radius at the tip of the stress raisers. As a consequence, the crack onset is controlled by energy criteria rather that the stress one. The slope characterising the scaling law depends upon the orientation, since the development of the process zone not only depends upon both the overall particle geometry and size but also on the local particle geometry near the stress raiser at which the decohesion is observed.

8. Conclusion

The effect of particle size on particle/matrix debonding has been studied using two different models: an analytical one (FFM) and a numerical one (CZM). First a spherical particle has been considered and two types of loading conditions have been applied: hydrostatic and uniaxial tension respectively. A clear particle size effect has been observed:

- For both models, the larger the particle, the smaller the critical load required to initiate particle debonding. This is in good accordance with experimental observations from the literature.
- Both models are based on two parameters: the critical energy release rate G_c and the strength σ_{max}. For both models two asymptotic behaviours are observed depending on the two parameters introduced:
  - For large particles, both models give a plateau value of the critical stress for debond onset. This value is reached when the stress at the interface exceeds its strength. This means that for large particles, the debonding process is governed by a stress criterion.
  - For small particles, different asymptotic behaviours are observed for the two models. The evolution of the critical stress that triggers debonding is proportional to $1/\sqrt{R}$ for the FFM-based model and proportional to $1/R$ for the CZM. For these small particles, the debonding process is governed by an energy criterion. The value $1/\sqrt{R}$ of the FFM is also in accordance to analytical energetic considerations previously made in the literature.
- The difference between FFM and CZM scaling laws is attributed to the presence of a large process zone prior to full debond, which is not taken into account with FFM analysis. Such mechanisms enhance the energy dissipation as well as the interface stiffness introduced in the CZM, which modifies the whole RVE behaviour for small particles.
- Both models show an intermediate behaviour for particles in the transition zone between the two asymptotic behaviours. The transition from one behaviour to the other can be estimated using a characteristic length, whatever the interface and materials properties of the model.

Those two models have then been applied to an angular particle situation, this geometry being more representative of the ones observed when ceramics (boron carbide, alumina, etc.) are used as reinforcements. The sharp corners have been smoothed with fillets in order to overcome stress singularity effects, whilst keeping large stress concentration values. A size effect similar to the one for spherical particles has been observed as large particles tend to debond prior to smaller ones. A different scaling law to the one observed for circular particle shapes is found, and several transition regimes are observed depending on particle orientation. Depending on the particle orientation, the crack onset is either triggered by the overall geometry or by the influence of local stress raisers around the particle, which tend to act as individual "particles". Individual treatment of the corner/sharp geometry should be undertaken when comparing the FFM approach with the CZM approach for more precise evaluation of the influence of process zone development on the locus of particle/matrix decohesion and remote critical stress value.

Acknowledgements

DGA of France, supporting the first author through *Allocation de thèse 2015*, is gratefully acknowledged.

References

[1] A. Gent, B. Park, Failure processes in elastomers at or near a rigid spherical inclusion, Journal of Materials Science 19 (6) (1984) 1947–1956.

[2] S. Fu, X. Feng, B. Lauke, Y. Mai, Effects of particle size, particle/matrix interface adhesion and particle loading on mechanical properties of particulate–polymer composites, Composites Part B: Engineering 39 (6) (2008) 933–961.

[3] S. Steffensen, R. Kibsgaard, H. Jensen, Debonding of particles in thin films, International Journal of Solids and Structures 51 (15-16) (2014) 2850–2856.

[4] J. Chen, M. Yuan, Decoupling of viscous dissipation and damage dissipation in particulate-reinforced polymeric materials, Computational materials science 40 (2) (2007) 267–274.

[5] J. Chen, Z. Huang, J. Zhu, Size effect of particles on the damage dissipation in nanocomposites, Composites Science and Technology 67 (14) (2007) 2990–2996.

[6] Y. Nakamura, M. Yamaguchi, M. Okubo, T. Matsumoto, Effect of particle size on the fracture toughness of epoxy resin filled with spherical silica, Polymer 33 (16) (1992) 3415–3426.

[7] J. Goodier, Concentration of stress around spherical and cylindrical inclusions and flaws, J. appl. Mech 1 (1) (1933) 39–44.

[8] J. Tjernlund, E. Gamstedt, P. Gudmundson, Length-scale effects on damage development in tensile loading of glass-sphere filled epoxy, International journal of solids and structures 43 (24) (2006) 7337–7357.

[9] B. Lauke, Effect of particle size distribution on debonding energy and crack resistance of polymer composites, Computational Materials Science 77 (2013) 53–60.

[10] A. Gent, Detachment of an elastic matrix from a rigid spherical inclusion, Journal of Materials Science 15 (11) (1980) 2884–2888.

[11] J. Williams, Particle toughening of polymers by plastic void growth, Composites science and technology 70 (6) (2010) 885–891.

[12] M. Zappalorto, M. Salviato, M. Quaresimin, Assessment of debonding-induced toughening in nanocomposites, Procedia Engineering 10 (2011) 2973–2978.

[13] M. Salviato, M. Zappalorto, M. Quaresimin, Nanoparticle debonding strength: A comprehensive study on interfacial effects, International Journal of Solids and Structures 50 (20) (2013) 3225–3232.

[14] M. Zappalorto, M. Salviato, M. Quaresimin, Influence of the interphase zone on the nanoparticle debonding stress, Composites Science and Technology 72 (1) (2011) 49–55.

[15] M. Zappalorto, M. Salviato, M. Quaresimin, Stress distributions around rigid nanoparticles, International Journal of Fracture (2012) 1–8.

[16] D. Leguillon, Strength or toughness? a criterion for crack onset at a notch, European Journal of Mechanics-A/Solids 21 (1) (2002) 61–72.

[17] P. Weißgraeber, D. Leguillon, W. Becker, A review of finite fracture mechanics: crack initiation at singular and non-singular stress raisers., Archive of Applied Mechanics 86.

[18] I. García, V. Mantič, E. Graciani, A model for the prediction of debond onset in spherical-particle-reinforced composites under tension. application of a coupled stress and energy criterion, Composites Science and Technology 106 (2015) 60–67.

[19] P. Cornetti, N. Pugno, A. Carpinteri, D. Taylor, Finite fracture mechanics: a coupled stress and energy failure criterion, Engineering Fracture Mechanics 73 (14) (2006) 2021–2033.

[20] E. Rybicki, M. Kanninen, A finite element calculation of stress intensity factors by a modified crack closure integral, Engineering Fracture Mechanics 9 (4) (1977) 931–938.

[21] J. Cho, M. Joshi, C. Sun, Effect of inclusion size on mechanical properties of polymeric composites with micro and nano particles, Composites Science and Technology 66 (13) (2006) 1941–1952.

[22] G. Alfano, M. Crisfield, Finite element interface models for the delamination analysis of laminated composites: mechanical and computational issues, International journal for numerical methods in engineering 50 (7) (2001) 1701–1736.

[23] I. García, V. Mantič, E. Graciani, Debonding at the fibre–matrix interface under remote transverse tension. one debond or two symmetric debonds?, European Journal of Mechanics-A/Solids 53 (2015) 75–88.

Tables

	$E\ [GPa]$	$\nu\ [\ ]$	$\sigma_{max}\ [MPa]$	$G_c\ [J.m^{-2}]$
Particle	450	0.2	$\times$	$\times$
Matrix	3	0.3	$\times$	$\times$
Interface	∞	$\times$	50	100

Table 1: Mechanical properties of the materials

Figures

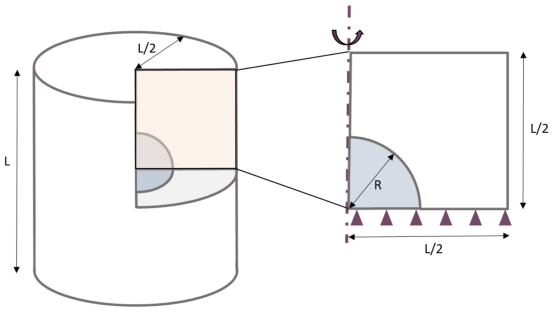

Figure 1: Spherical particle embedded in a cylindrical matrix; geometric reduction of the problem using symmetries.

(a) (b)

Figure 2: (a) Load-displacement curves of an elastic system before (blue) and after (orange) crack propagation;
(b) Pressure-dilatation curves of an elastic system before (blue) and after (orange) crack propagation.

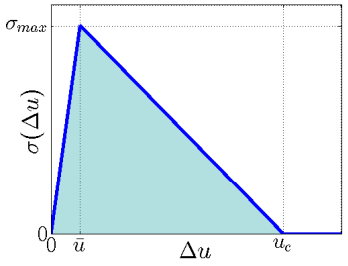

Figure 3: Bilinear Cohesive Zone Model.

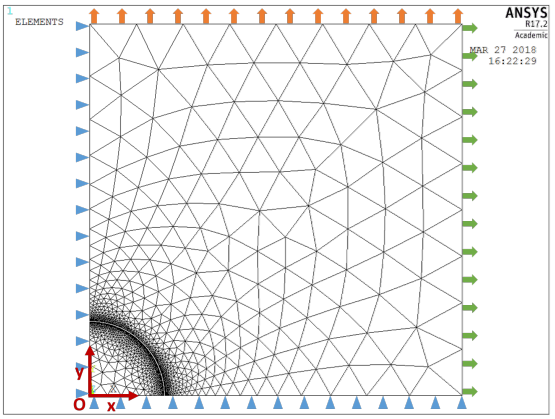

Figure 4: Geometry, mesh and loading conditions of the spherical particle debonding study with the CZM.

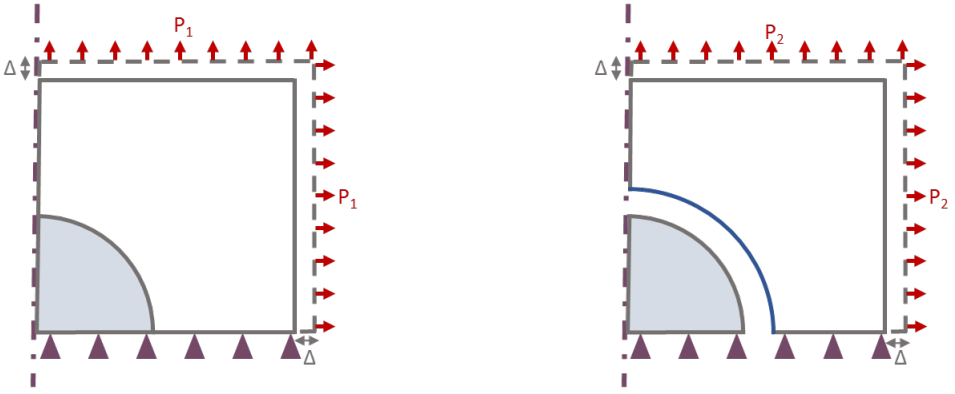

(a) (b)

Figure 5: (a) Debonding of the particle under hydrostatic tensile loading before crack propagation: the interface is perfectly bonded;
(b) Debonding of the particle under hydrostatic tensile loading after crack propagation: the particle is completely debonded.

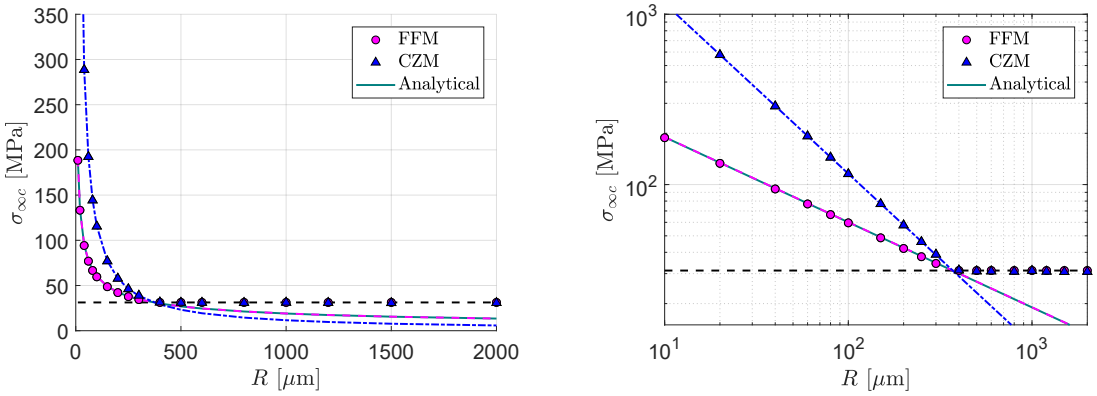

(a) (b)

Figure 6: (a) Critical remote stress responsible for first debond against particle radius under hydrostatic tension;
(b) Critical remote stress responsible for first debond against particle radius in logarithmic scale under hydrostatic tension.

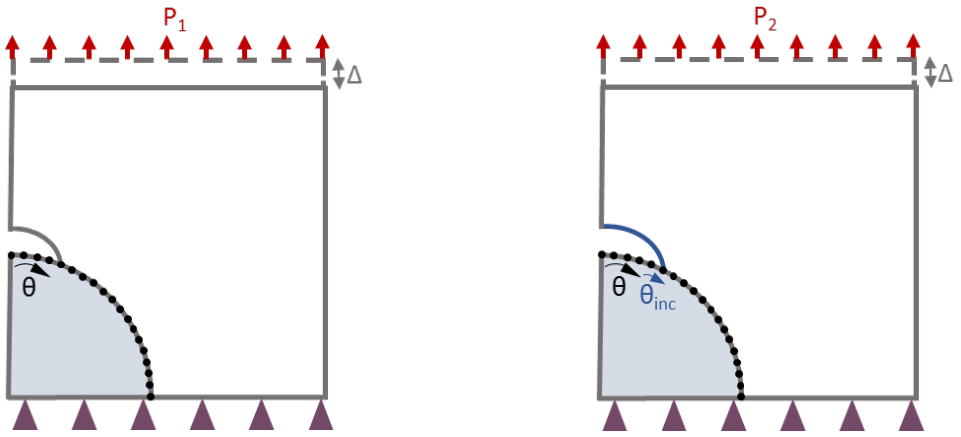

(a) (b)

Figure 7: (a) Debonding of the particle under uniaxial tensile loading, the crack tip is at an angle θ;
(b) Debonding of the particle under uniaxial tensile loading, the crack tip is at an angle $\theta + \theta_{inc}$.

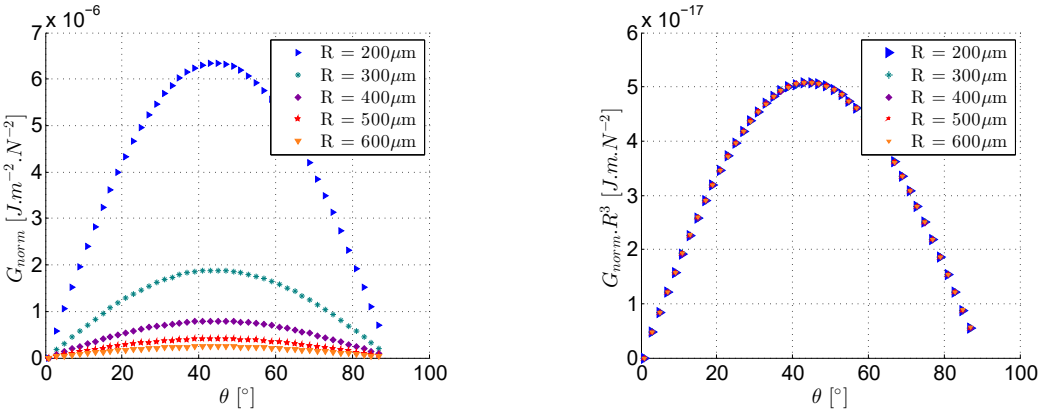

(a) (b)

Figure 8: (a) Normalised energy release rate against debonding angle for different particle sizes;
(b) Normalised energy release rates against debonding angle equalised for all the particle sizes.

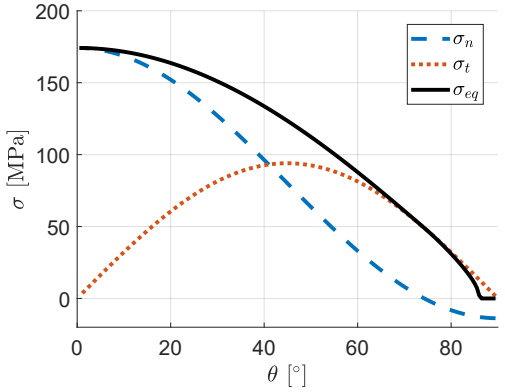

Figure 9: Local stress fields around the particle (for an arbitrary remote stress of 90 MPa).

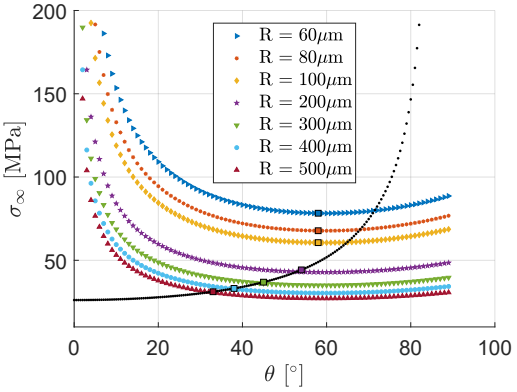

Figure 10: Remote critical stress against debonding angle for the energy and the stress criteria for different particle sizes.

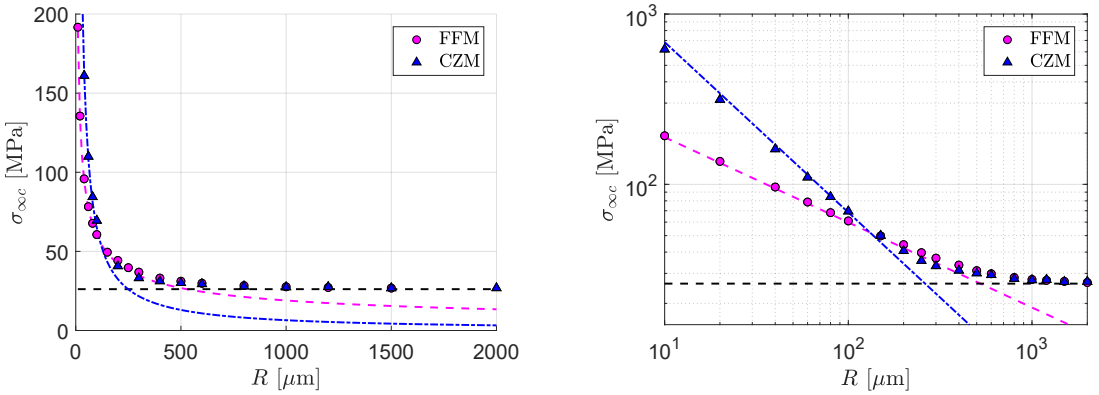

Figure 11: (a) Critical remote stress responsible for first debond against particle radius under uniaxial tension;
(b) Critical remote stress responsible for first debond against particle radius in logarithmic scale under uniaxial tension.

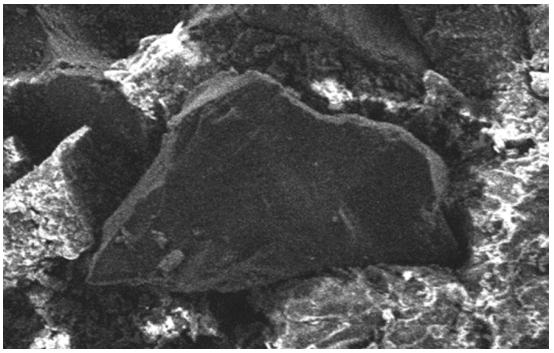

Figure 12: Boron Carbide (B_4C) particle embedded in the epoxy matrix observed with SEM.

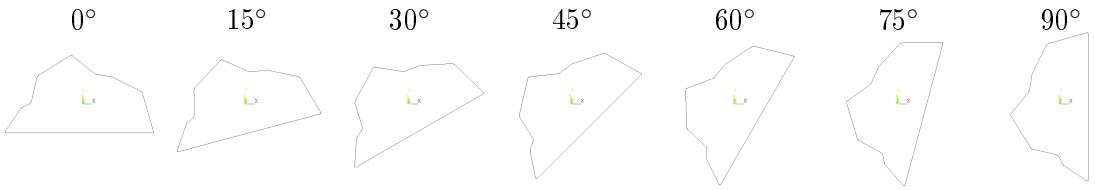

Figure 13: Rotations of the angular particle from 0° to 90°.

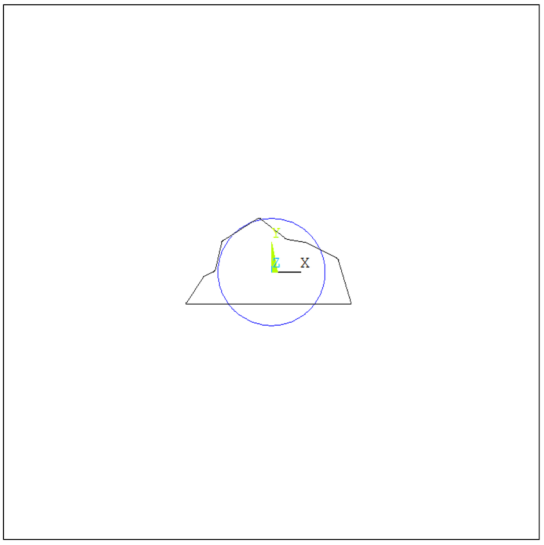

Figure 14: Geometries of embedded particle (circular and angular).

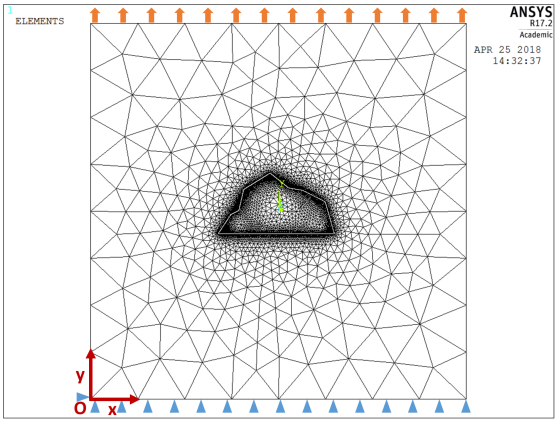

Figure 15: Geometry, mesh and loading conditions of the angular particle debonding study with the CZM.

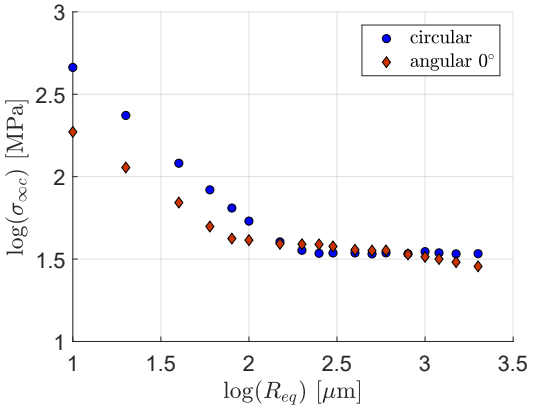

Figure 16: Critical remote stress against particle (equivalent) radius for the circular and angular (0° rotation) particles.

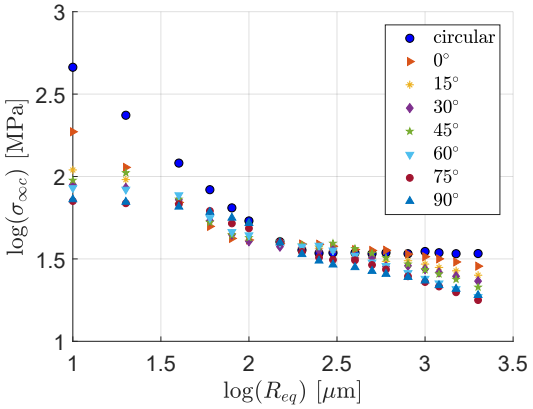

Figure 17: Critical remote stress against particle (equivalent) radius for the circular and all the angular (0° to 90° rotation) particles.

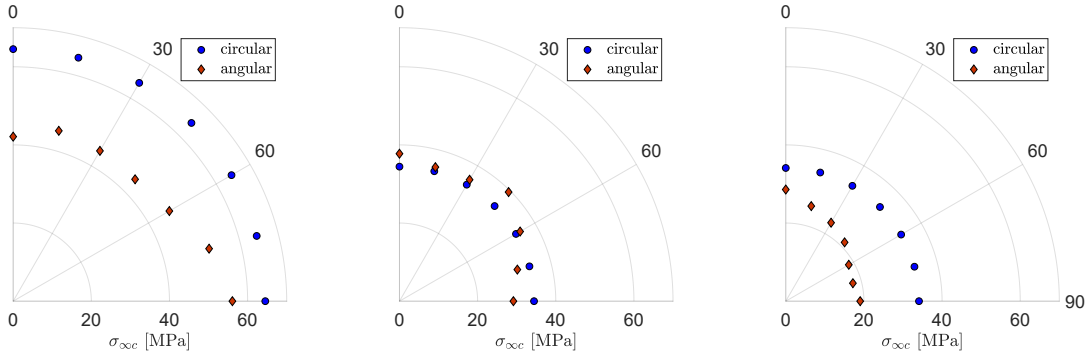

Figure 18: Critical remote stress against rotation angle for angular particles ((a) $R_{eq} = 80\mu m$, (b) $R_{eq} = 300\mu m$, (c) $R_{eq} = 2000\mu m$)